Article

Mixed Anion Control of the Partial Oxidation of Methane to Methanol on the β-PtO$_2$ Surface

Yuta Tsuji,* Keita Kurino, and Kazunari Yoshizawa*

Read Online

ACCESS | Metrics & More | Article Recommendations | SI Supporting Information

ABSTRACT: Although the C−H bond of methane is very strong, it can be easily dissociated on the (110) surface of β-PtO$_2$. This is because a very stable Pt−C bond is formed between the coordinatively unsaturated Pt atom and CH$_3$ on the surface. Owing to the stable nature of the Pt−C bond, CH$_3$ is strongly bound to the surface. When it comes to methanol synthesis from methane, the Pt−C bond has to be cleaved to form a C−O bond during the reaction process. However, this is unlikely to occur on the β-PtO$_2$ surface: The activation energy of the process is calculated to be so large as 47.9 kcal/mol. If the surface can be modified in such a way that the ability for the C−H bond activation is maintained but the Pt−C bond is weakened, a catalyst combining the functions of C−H bond cleavage and C−O bond formation can be created. For this purpose, analyzing the orbital interactions on the surface is found to be very useful, resulting in a prediction that the Pt−C bond can be weakened by replacing the O atom trans to the C atom with a N atom. This would be a sort of process to make β-PtO$_2$ a mixed anion compound. Density functional theory simulations of catalytic reactions on the β-PtO$_2$ surface show that the activation energy of the rate-limiting step of methanol synthesis can be reduced to 27.7 kcal/mol by doping the surface with N.
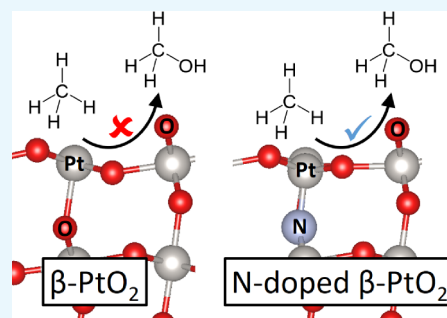
1. INTRODUCTION

Methane is abundant on earth in a variety of forms, including natural gas, shale gas, coalbed methane, biogas, and methane hydrates.[1] The direct conversion of methane into a liquid chemical such as methanol, suitable for transportation and storage, is highly desirable because of its industrial importance.[2−4] In the conventional route of the industrial synthesis of methanol, methane is first reformed into syngas, a gas mixture consisting primarily of hydrogen (H$_2$) and carbon monoxide (CO), and then converted to methanol.[5] The step of converting methane to syngas requires a Ni catalyst, and this reaction typically proceeds at a temperature of about 850 °C and a pressure of about 2.5 MPa.[6] The step of catalytically synthesizing methanol from syngas also requires high-temperature and high-pressure conditions of 250−300 °C and 5−15 MPa, respectively. ZnO/Cr$_2$O$_3$ was used as a catalyst in the early days, but more recently, Cu catalysts have been used in most commercial processes.[7] Owing to the high-temperature and high-pressure reaction conditions, these chemical processes are costly. The development of methods for the direct conversion of methane to methanol under mild conditions could lead to major commercial breakthroughs in the use of methane.

The reason why the conventional conversion of methane requires high-temperature and high-pressure conditions can be attributed to the fact that the dissociation energy of the C−H bond of methane is as large as 104 kcal/mol.[2] Compared with the strength of the C−H bond of other alkanes, that of methane is found to be significantly large.[2] However, the activation energy required for the dissociation of the methane's C−H bond is very low on the surface of some late transition-metal oxides, such as IrO$_2$, RuO$_2$, and PdO.[8,9] In particular, the reactivity of IrO$_2$ is remarkable because it was experimentally observed that the dissociation of the methane's C−H bond occurs on the IrO$_2$ (110) surface at a low temperature of 150 K.[10] However, it is to be regretted that methanol cannot be synthesized on the surface of such a metal oxide.

Weaver and co-workers carried out a thorough study on the oxidation of methane on the IrO$_2$ (110) surface using temperature-programmed reaction spectroscopy (TPRS) and density functional theory (DFT).[11] Its TPRS spectra indicated that the activation of methane on the stoichiometric IrO$_2$ surface results in the competition between the oxidation of methane to CO and CO$_2$ and the recombination of the CH$_3$ and H species. Its DFT calculations suggested that the rate-limiting step in the oxidation of methane is C−O bond formation, the activation barrier of which is in the range of 32−39 kcal/mol, almost comparable with that for the combinative generation of methane (29 kcal/mol). The high activation barrier of C−O bond formation on the IrO$_2$ surface may be
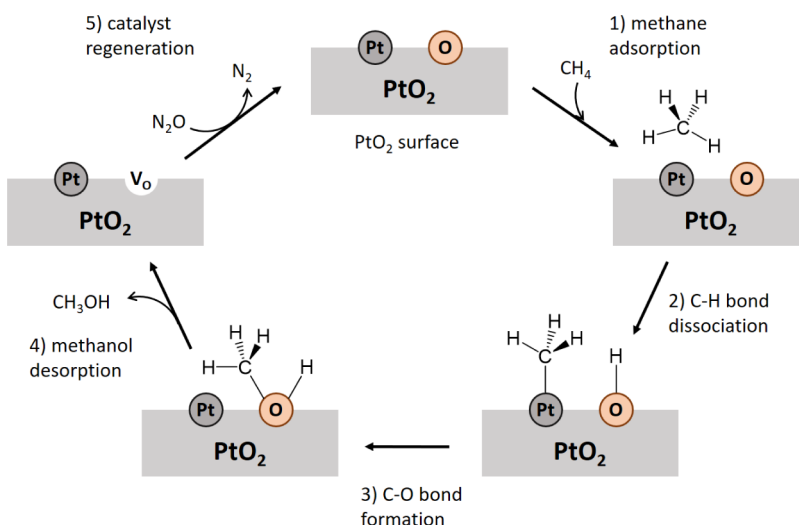
Figure 1. Proposed Mars−van Krevelen-type catalytic cycle for the direct conversion of methane to methanol on the surface of PtO_2. V_O denotes the oxygen vacancy, which is replenished by the reaction with N_2O.

due to the strong binding of the oxygen atom to underlying surface Ir atoms. A high temperature of about 500 K is required for these reactions.

Rui and co-workers reported a bicomponent catalyst, IrO_2/CuO, for the direct oxidation of methane to methanol under mild conditions.[12] In their study, the synergetic function of IrO_2 for methane activation and CuO for selective oxidation was identified. They hypothesized that metal oxides with a weak metal−O (M−O) bond strength should be beneficial for C−O bond formation and methanol extraction, when employed as a cocatalyst with IrO_2.

The heat of formation of metal oxides may be a good measure of M−O bond strength.[13] According to the Materials Project database,[14] the heat of formation of IrO_2, or the reaction enthalpy for $Ir + O_2 \rightarrow IrO_2$, is −88 kcal/mol. Since the heat of formation of PtO_2 is −65 kcal/mol, Pt−O bonds are expected to be weaker than Ir−O bonds. It would be of interest to note that, in our previous study, we theoretically predicted that PtO_2 is more active for the C−H bond dissociation of methane than IrO_2.[15] Therefore, PtO_2 may have two advantages such as the reactivity toward CH_4 and weak M−O bond strength, respectively, identified for IrO_2 and CuO in the bicomponent catalyst of IrO_2/CuO. In this paper, we will theoretically probe the possibility of using PtO_2 as a catalyst for the direct conversion of methane to methanol.

Many studies on the oxidation of methane on late transition-metal surfaces have revealed that methane is oxidized through reaction with oxygen atoms located on the catalyst surface (surface lattice oxygen atoms), after which oxygen vacancies (V_O) are left behind on the surface.[11,16,17] Such a reduced metal-oxide surface can be restored to its initial state by the reoxidation of the catalyst to complete the catalytic cycle. This is the so-called Mars−van Krevelen mechanism,[18] which is often used to describe the oxidation of hydrocarbons on heterogeneous metal-oxide catalysts.[19−21]

Figure 1 shows a catalytic cycle to be proposed for the direct conversion of methane to methanol on the surface of PtO_2 in the Mars−van Krevelen mechanism. First, a pair of Pt and O atoms on the surface dissociates a C−H bond of methane, forming CH_3* and $OH*$ species on the surface, where * denotes adsorbed species. The following C−O bond formation results in CH_3OH*, the desorption of which leaves an oxygen

vacancy (V_O) behind the surface. Finally, the V_O site is replenished by an oxygen atom supplied by a gaseous N_2O molecule.

As we will see, our DFT calculations indicate that the step of C−O bond formation is the rate-limiting step with a relatively large activation barrier. To lower the activation barrier and propose a more practical catalyst, we adopt the concept of mixed-anion compounds, a series of materials containing multiple anionic species in a single solid-state phase.[22,23]

In our previous study,[24] we demonstrated that it is possible to tune the height of the activation barrier for the first C−H bond cleavage reaction of methane on the IrO_2 surface by replacing an oxide with a different anion. We may term this process as doping. In this study, the same strategy is employed to reduce the activation barrier of C−O bond formation on the PtO_2 surface. As a result, the doping of N into PtO_2 turns out to be beneficial for the synthesis of methanol from methane. In the previous study, we focused on a single elementary reaction and tried to control its activation energy. However, in this study, we focus on the entire catalytic cycle and try to optimize the catalytic reaction by controlling the activation energy of its rate-limiting step.

2. THEORETICAL METHODS

2.1. Construction of a Model Structure. Experimental studies have reported the presence of three polymorphs for PtO_2: α-PtO_2 (hexagonal CdI_2-type structure),[25,26] β-PtO_2 (orthorhombic $CaCl_2$-type structure),[25,27] and β'-PtO_2 (tetragonal rutile-type structure).[28] Preceding theoretical studies using DFT on the electronic energy calculations of these three phases have established that the total energy calculated at 0 K increases in the order of β-$PtO_2 \lesssim \alpha$-$PtO_2 < \beta'$-PtO_2.[29−32] The energy difference between β-PtO_2 and α-PtO_2 is no larger than 0.02 eV/f.u.[29,30,32] The structures of α-PtO_2 and β-PtO_2 are compared in the Supporting Information. Experimentally, the phase of β-PtO_2 is prepared under high temperatures and high oxygen pressures;[25] β-PtO_2 has been reported to be stable at high temperatures and high pressures.[28,29]

Owing to the disagreement between theory and experiment, the relative stability between α-PtO_2 and β-PtO_2 is still a matter of debate. The stability of the phases of PtO_2 has been

investigated based on first-principles methods to calculate the Gibbs free energy. In 2006, Zhuo and Sohlberg[29] reported that the α phase is thermodynamically stable at low pressures, while the β phase is stable at high pressures, whereas in 2020, Chen and Yang[31] reported that the β phase is the most stable within a wide range of temperature (0–600 K) and pressure (0–51 GPa). We ourselves performed frozen phonon calculations for the α and β phases to evaluate how large the free-energy difference is. The results are shown in the Supporting Information. Here, just briefly, the free-energy difference is no larger than 0.004 eV/f.u. in the investigated temperature range (0–1000 K). However, it is worth noting that the β phase is slightly more stable than the α phase at high temperatures where catalytic reactions may occur.

Although whether β-PtO$_2$ exists under ambient conditions may be a moot question, in this study, we adopted the structure of β-PtO$_2$ for a model of PtO$_2$. This is because the CaCl$_2$-type structure of β-PtO$_2$ can be viewed as an orthorhombic distortion of the rutile structure,[28] and methane activation on the surface of rutile-type metal dioxides has been extensively investigated.[8–11,15,24]

The crystal structure of β-PtO$_2$ was optimized using DFT, as implemented in Vienna ab initio simulation package (VASP) 5.4.1.[33–36] The generalized gradient approximation was adopted with the functional described by Perdew, Burke, and Ernzerhof (PBE).[37] The Kohn–Sham equations were solved with a plane-wave basis set using the projector-augmented wave method.[38,39] The cutoff energy for the plane-wave basis set was set to 500 eV. A Gaussian smearing with a width of σ = 0.05 eV for the occupation of the electronic levels was used. The convergence threshold for self-consistent field iteration was set to 1.0×10^{-6} eV. The atoms in the slab model were relaxed until the forces on all of the atoms are less than 0.03 eV/Å. The Γ-centered k-point meshes with k spacing of $2\pi \times 0.05$ Å^{-1} were employed for sampling the Brillouin zone. Spin-polarization calculations were performed for all of the systems.

Shannon reported the semiconductive properties of β-PtO$_2$ based on its resistivity measurement.[27] Yang et al.[40] conducted a theoretical study using the single-shot GW (G$_0$W$_0$) approach, reporting a calculated band gap of 1.25 eV. They also reported that the DFT plus Hubbard U (DFT + U) method can reproduce the G$_0$W$_0$-calculated band gap when the effective on-site Coulomb repulsion parameter U_{eff} is set to 7.5 eV for Pt 5d states. Using this U_{eff} value, we have conducted Dudarev's method[41] of DFT + U calculations for β-PtO$_2$.

Figure 2 shows the optimized bulk structure of β-PtO$_2$. This structure is visualized using VESTA.[42] We will use this software throughout this study for visualizing structures. The
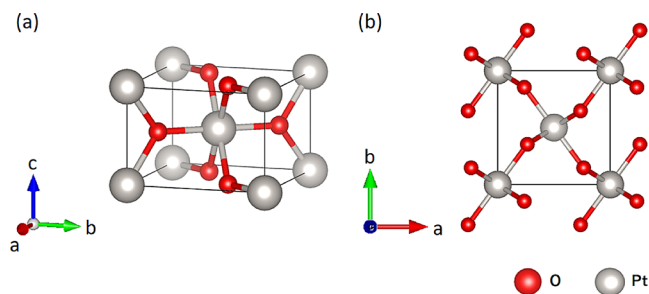

Figure 2. Optimized bulk structure of β-PtO$_2$, which is viewed along the standard orientation of the crystal shape (a) and from the c axis onto the ab plane (b).

optimized cell parameters of β-PtO$_2$ are listed in the Supporting Information. They show a good agreement with those obtained in the experiment.

As a model for the surface of β-PtO$_2$, the (110) and (001) surfaces have been used in previous theoretical studies.[43–46] Hu and co-workers investigated CO oxidation on PtO$_2$ using DFT calculations, stating that (110) is the most stable surface and suitable for the modeling of the catalyst surface.[47] Using a thermodynamics approach together with DFT calculations, Jacob showed the preference for the formation of the β-PtO$_2$ (110) surface on Pt electrodes in electrochemical environments.[48] As for rutile, the (110), (001), and (100) surfaces have been well characterized, of which the (110) is the most stable.[49] The structure of β-PtO$_2$ can be viewed as a distorted rutile structure, and methane activation on the (110) surface of rutile-type late transition-metal dioxides has been extensively studied.[8–10] Thus, we adopted the (110) facet as a model for the surface of β-PtO$_2$ in this study.

A slab model for the (110) surface of β-PtO$_2$ was constructed and optimized, as shown in Figure 3. The created
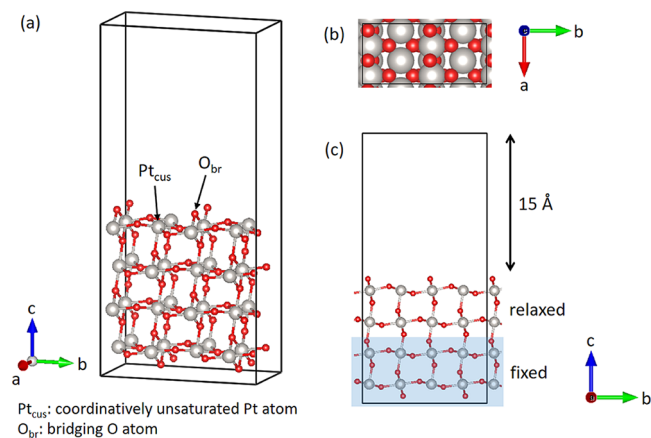

Figure 3. Optimized slab model structure for the (110) surface of β-PtO$_2$, which is viewed along the standard orientation of the crystal shape (a), from the c axis onto the ab plane (top view) (b), and from the a axis onto the cb plane (side view) (c). (a) and (c) are shown in a ball-and-stick model, while (b) is shown in a space-filling model. A vacuum space of 15 Å length is placed on the surface. The coordinates of the atoms in the shaded region in the side view (c) are kept fixed during optimization.

slab model has a 2 × 2 surface in the unit cell with the thickness of four O–Pt–O repeating units. The lowest two layers were fixed during the geometry optimization. A 15 Å thick vacuum layer was placed on the surface. The other calculation conditions were set to be the same as those used for the bulk calculation mentioned above.

On the (110) surface of β-PtO$_2$, one can see alternating rows of 2-fold coordinated bridging O atoms (O$_{\text{br}}$) and 5-fold coordinatively unsaturated Pt atoms (Pt$_{\text{cus}}$). In methane activation, the O$_{\text{br}}$ atom will abstract a H atom from methane, and the CH$_3$ species thus generated will be adsorbed onto the Pt$_{\text{cus}}$ atom.

2.2. Search for Transition-State Structures. To obtain the minimum energy path and the transition-state structure for each step in the catalytic cycle proposed in Figure 1, we performed the climbing image-nudged elastic band (CI-NEB) method,[50–52] as implemented in VASP through the VTST Tools.[53] The spring constant between adjacent NEB images
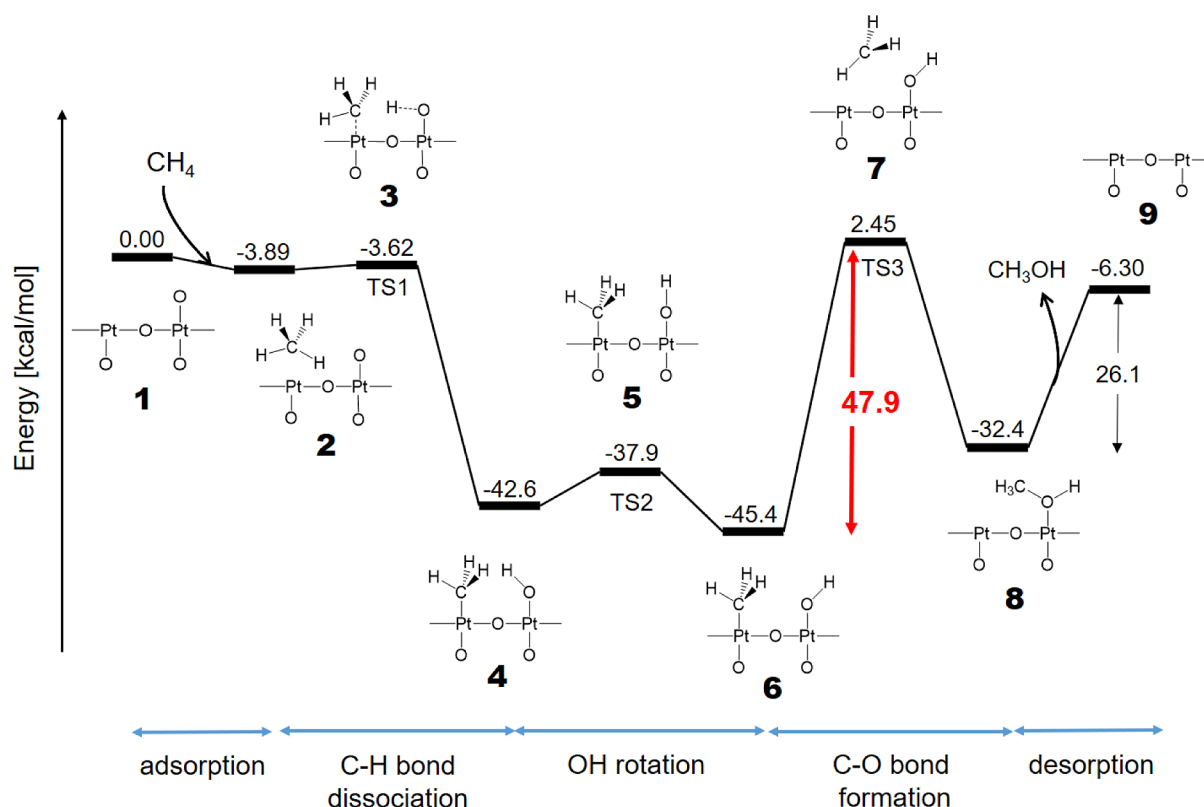
Figure 4. Calculated energy diagram for methanol synthesis on the (110) surface of β-PtO$_2$. The structures are drawn in a schematic way to help one clearly understand what is going on. The numbers shown above the black bold horizontal lines representing intermediate states are their energies (in kcal/mol), which are calculated by taking the energy of the initial state as a reference. The activation barrier of the rate-limiting step is highlighted by red. The structures are sequentially numbered in the order of their appearance in the reaction.

was set to 5.0 eV/Å. The quasi-Newton algorithm[54] implemented in VASP was adopted for the geometry optimization of all of the NEB images. The other calculation conditions were set to be the same as those used for the bulk calculation mentioned above.

2.3. Analysis of Electronic Structures. There may be some ways to approach the electronic aspect of the catalytic activity of β-PtO$_2$. In this study, we have made good use of a powerful band-decomposition tool called crystal orbital overlap population (COOP).[55,56] COOP can be viewed as a partial density of states for a pair of atoms weighted with the corresponding Mulliken overlap population.[57,58] COOP is plotted as a function of energy, providing a simple graphical representation as to whether the interaction between the pair of atoms exhibits a bonding character or antibonding one at a certain energy level: positive COOP values indicate bonding interactions, while negative values indicate antibonding interactions.

In this study, the COOP calculations were carried out by using the extended Hückel (eH) program of YAeHMOP,[59] as implemented in Avogadro software.[60] The standard atomic parameters used were taken from the literature,[61] as tabulated in the Supporting Information. The same *k* spacing as used in the DFT calculations was used. One could conduct the same calculation at the DFT level, but we performed at the eH level. This is because in our previous studies on methane activation on metal oxides,[15,24,62] we have confirmed that these two methods generally provide results with the same trend.

To identify COOP peaks, we performed a fragment molecular orbital (FMO) analysis, as implemented in

YAeHMOP.[59] Since this analysis cannot directly be applied to systems with periodic boundary conditions, we cut out a cluster from the optimized slab model and performed FMO calculations for the cluster model. FMO diagrams were drawn with Viewkel.[63] The isosurfaces of eHMOs were generated using the QuantumWise Atomistix ToolKit (QuantumATK) 2019 package[64] and visualized using VESTA.

3. RESULTS AND DISCUSSION

3.1. Methanol Synthesis on the Surface of β-PtO$_2$. Figure 4 shows the calculated energy diagram for methanol synthesis on the (110) surface of β-PtO$_2$. For simplicity, the structures are shown in a schematic manner. Their optimized atomic coordinates are shown in the Supporting Information, and some of them will be discussed more in detail later in this paper.

Let us explain what occurs on the surface in words. The first step is the adsorption of methane followed by the C−H bond dissociation reaction. The adsorption structure as well as the transition-state structure for the dissociation has already been investigated and discussed in detail in our previous publication.[15] We will touch briefly on these steps.

The adsorption energy of methane on the β-PtO$_2$ surface is about −3.9 kcal/mol, slightly larger in magnitude than that on the Pt (111) surface (ca. −3.4 kcal/mol).[65] The activation barrier to dissociation from the molecularly adsorbed state is as low as about 0.3 kcal/mol, much smaller than that on the IrO$_2$ (110) surface (ca. 6.8 kcal/mol).[10] Judging from the adsorption and activation energies calculated and the values from the relevant experiments, the dissociative chemisorption
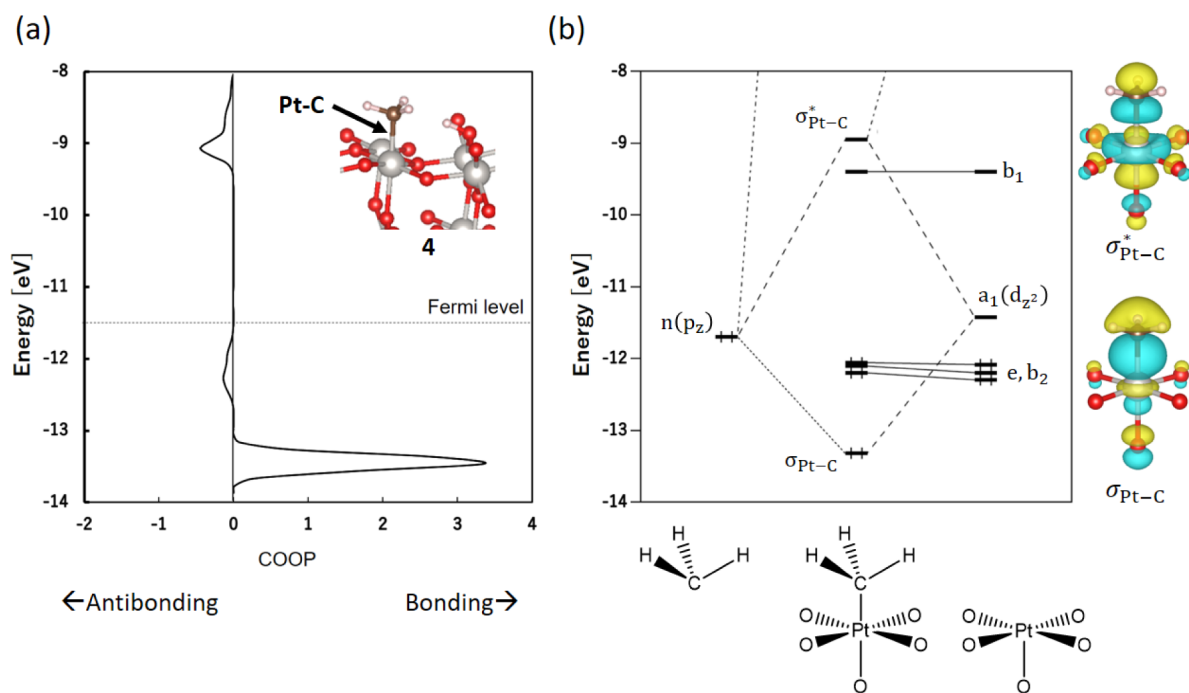
Figure 5. (a) COOP curve for the $Pt_{cus}-CH_3$ bond on the surface in the structure of **4**. In the inset, the bond calculated is pointed by an arrow. The dotted line indicates the Fermi level. (b) FMO interaction diagram for the formation of the cluster of $[Pt(CH_3)O_5]^{7-}$ from the CH_3^- and $[PtO_5]^{6-}$ fragments. The eH-calculated σ_{Pt-C} and σ_{Pt-C}^* orbitals are visualized, with the isosurface value set to 0.05 $e^{1/2}/a_0^{3/2}$. The symmetry labels used for the orbitals of the PtO_5 fragment correspond to those for square-pyramidal C_{4v} symmetry for simplicity, though in reality the fragment structure is distorted from the square pyramid. A qualitative understanding of the generation of the fragment orbitals for $[PtO_5]^{6-}$ is presented in the Supporting Information.

of methane on the β-PtO_2 surface occurs readily even at low temperatures.

The rotation of the OH group, which is generated as a result of the H atom abstraction from methane by the O_{br} atom, will follow the dissociative chemisorption of methane. This reaction is almost thermoneutral, and its activation barrier is not large (4.7 kcal/mol). This step may be deemed a trivial step.

Let us turn to the important process of C–O bond formation, which would occur after the OH rotation. The calculated activation barrier of this step is as large as 47.9 kcal/mol. If this barrier is overcome, the release of methanol would occur with a moderate desorption barrier of about 26 kcal/mol. By and large, this desorption barrier is smaller than the energy required for methanol desorption from the active site of the typical catalysts of Fe- and Cu-exchanged zeolites.[66]

The highest energy barrier that must be overcome in the course of the reaction is the barrier to TS3, so converting **6** to **8** via **7** is likely to be the rate-limiting step. To facilitate the methanol synthesis on the β-PtO_2 surface, we will try to make this energy barrier lower in the remaining part of this paper. First, we will analyze the electronic structure of **6** (or **4**) to gain an insight into the amelioration of the catalyst.

3.2. Electronic Structure Analysis. By looking over the whole potential energy profile associated with the reaction of converting methane to methanol on the β-PtO_2 surface, one can perceive that the high activation barrier to TS3 has something to do with a substantial stabilization of the CH_3 group on the surface. One can notice that there is a deep valley in the potential energy profile, the bottom of which includes structures **4**, **5**, and **6**. The significant affinity of the Pt_{cus} atom for CH_3 can be effective in promoting the initial C–H bond

dissociation of methane, but CH_3 is too strongly bound to the surface to be transferred to the OH group. This is why we will analyze the $Pt_{cus}-CH_3$ bond to trace the origin of the strong binding and will ponder on how to reduce the strength of the interaction.

Figure 5a shows the COOP curve for the $Pt_{cus}-CH_3$ bond on the surface of structure **4**. Even if one uses the structure of **6** instead, almost the same plot will be obtained. The positive and negative regions in the curve indicate bonding and antibonding interactions, respectively. A substantially high positive peak can be spotted at around $E = -13.5$ eV. Such a significant Pt–C bonding interaction is likely to be the cause of the strong binding of the CH_3 group to the surface.

To see by what kind of orbital interaction the bonding peak is generated, let us analyze the orbital interaction on the surface. As our modus operandi,[15,24,62] the part of PtO_5-CH_3 is cut out from **4** to generate a cluster model and an FMO analysis is carried out for the cluster, as shown in Figure 5b. In the orbital interaction diagram, one can clarify how the orbitals of the cluster model can be built up from those of the fragments of CH_3^- and $[PtO_5]^{6-}$. One can see a clear correspondence between the COOP curve and the orbital interaction diagram: The positive COOP peak at around $E = -13.5$ eV and the negative one at around $E = -9.1$ eV can be assigned to the σ_{Pt-C} and σ_{Pt-C}^* orbitals, respectively. Thus, the strong binding of the CH_3 group to the surface can be traced back to the formation of the σ_{Pt-C} orbital. Note that the energy levels in the COOP curve very precisely corresponding to those in the FMO result because both of them were calculated at the same theoretical level, namely, the eH method, where the same atomic parameters were used.
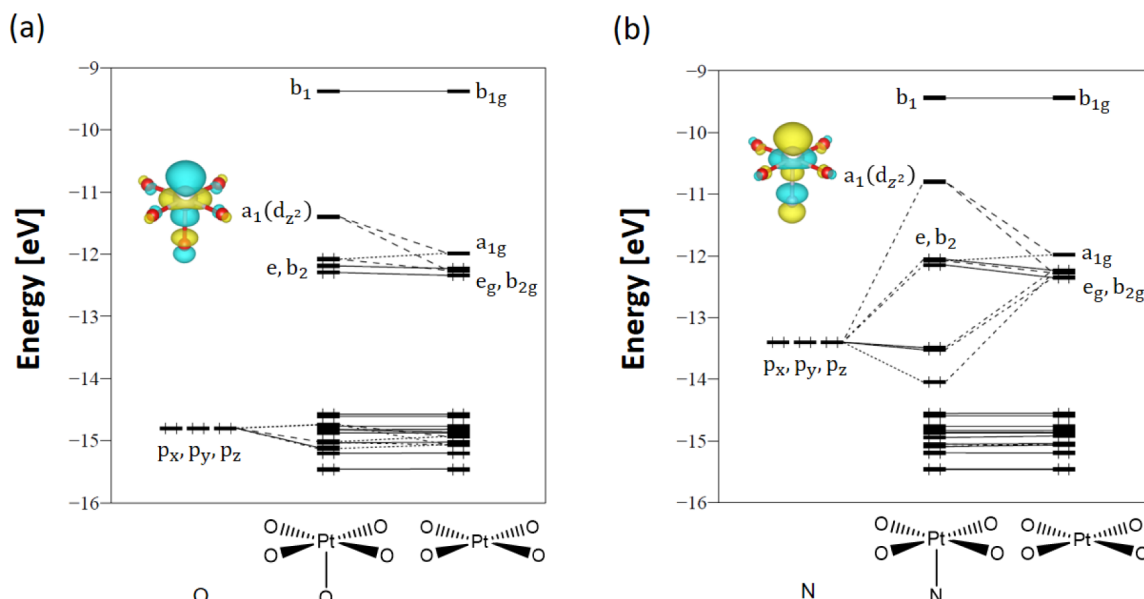
(a)

(b)

Figure 6. (a) FMO interaction diagram for the formation of the $[PtO_5]^{6-}$ fragment in Figure 5b from the $[PtO_4]^{4-}$ fragment and the axial O^{2-} ligand. The eH-calculated $a_1(d_{z^2})$ orbital is visualized, with the isosurface value set to 0.05 $e^{1/2}/a_0^{3/2}$. The symmetry labels used for the orbitals of the PtO$_4$ fragment correspond to those for square planar D_{4h} symmetry for simplicity, though in reality the fragment structure is distorted from the square plane. (b) FMO diagram revised after replacing the axial O ligand with a N ligand.

What we intend to do is to weaken the interaction between the CH$_3$ group and the surface so that the bottom of the valley in the potential energy profile can be raised. All we may need to do is to make the stabilized σ_{Pt-C} orbital destabilized. Let us see how it works, first with the eH method and then with DFT.

The σ_{Pt-C} orbital originates from the bonding interaction between the $n(p_z)$ orbital of CH$_3$ and the $a_1(d_{z^2})$ orbital of PtO$_5$. The $n(p_z)$ orbital is primarily derived from the 2p$_z$ orbital of the C atom though there is a tiny contribution from the 1s orbitals of the H atoms, while the $a_1(d_{z^2})$ orbital is formed by the contribution of the 2p$_z$ orbital of the axial O ligand to the 5d$_{z^2}$ orbital of the Pt atom. The formation of the $a_1(d_{z^2})$ orbital is analyzed, as shown in Figure 6a. Although Viewkel does not draw any line between the $a_1(d_{z^2})$ orbital and the 2p$_z$ orbital of the axial O ligand, it is clear from the isosurface plot for the $a_1(d_{z^2})$ orbital in the inset that the antibonding interaction between the a_{1g} orbital of PtO$_4$ and the 2p$_z$ orbital is the main component of the $a_1(d_{z^2})$ orbital.

There may be some ways to destabilize the σ_{Pt-C} orbital; one way to approach it is to make the $a_1(d_{z^2})$ orbital destabilized. As we have seen in Figure 6a, the antibonding interaction of the 2p$_z$ orbital of the axial O atom with the a_{1g} orbital results in the $a_1(d_{z^2})$ orbital; therefore, by pushing up the energy level of the 2p$_z$ orbital, the resultant $a_1(d_{z^2})$ orbital level will also go up. But how? If we are allowed to replace the axial O atom with a more electropositive element, say N, what we want to achieve will be achieved (see Figure 6b). The general concept behind this has already been detailed in our previous paper.[24]

By replacing the axial O ligand with the N ligand, which is what we call doping, the energy level of the 2p manifold of the ligand is increased, and in accordance with it, the energy of the $a_1(d_{z^2})$ orbital level becomes higher by about 0.6 eV. In Figure 7, one can see that the rise of the energy of the $a_1(d_{z^2})$ orbital leads to the destabilization of the σ_{Pt-C} orbital. Before the doping of N (Figure 5b), the σ_{Pt-C} orbital was located at $E =$
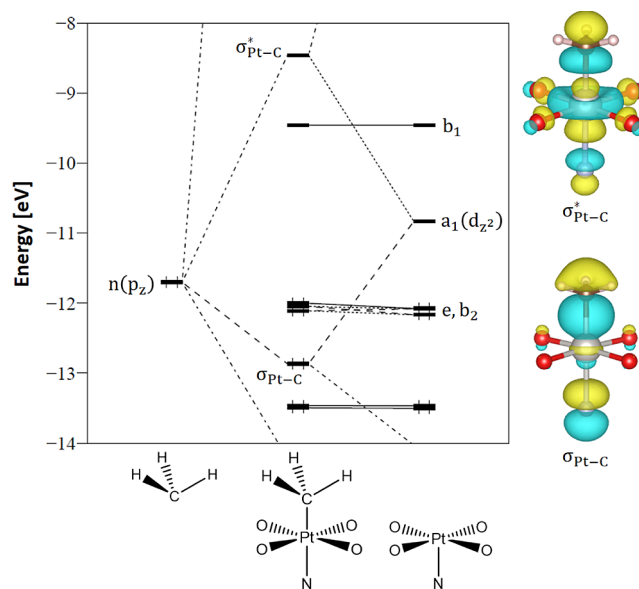

Figure 7. Molecular orbitals calculated for the cluster of $[Pt(CH_3)-NO_4]^{8-}$, which is generated by replacing the axial O ligand of the $[Pt(CH_3)O_5]^{7-}$ cluster with N, decomposed into the contributions from the orbitals of the CH$_3^-$ and $[PtNO_4]^{7-}$ fragments (FMO interaction diagram). The eH-calculated σ_{Pt-C} and σ_{Pt-C}^* orbitals are visualized, with the isosurface value set to 0.05 $e^{1/2}/a_0^{3/2}$.

−13.3 eV, while after the doping (Figure 7), the orbital is found at $E = -12.9$ eV.

3.3. Methanol Synthesis on the Surface of N-Doped β-PtO$_2$. Let us see how effective it is to dope the β-PtO$_2$ surface with N for methanol synthesis. We constructed a slab model for DFT calculations of the surface of N-doped β-PtO$_2$ by replacing the axial O ligand of one Pt$_{cus}$ atom with N. Using the same method as used to obtain Figure 4, we have obtained an energy diagram for methanol synthesis on the (110) surface of N-doped β-PtO$_2$, as shown in Figure 8.
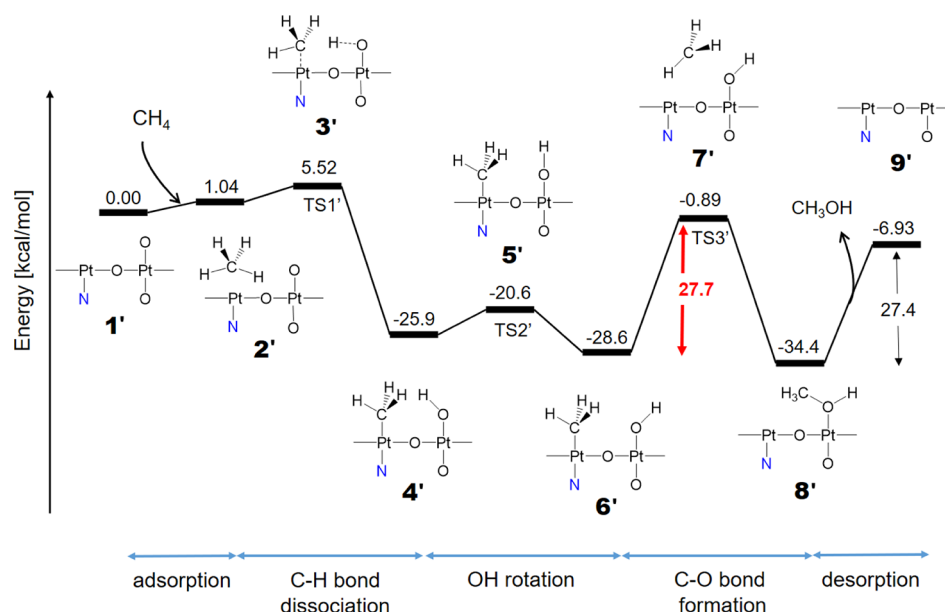
Figure 8. Calculated energy diagram for methanol synthesis on the (110) surface of N-doped β-PtO$_2$. The structures are drawn in a schematic way to help one understand what is going on clearly. The numbers shown above the black bold horizontal lines representing intermediate states are their energies (in kcal/mol), which are calculated by taking the energy of the initial state as a reference. The activation barrier of the rate-limiting step is highlighted with red. The structures are numbered in accordance with those in Figure 4 but distinguished from them using the prime symbol.

Comparing Figure 8 with Figure 4, one can notice a significant difference in the height of the activation barrier to TS3 (TS3′). By introducing a N atom into the subsurface site, the activation barrier of the rate-limiting step is reduced by about 20 kcal/mol, though the effect of N doping on the other activation barriers is relatively small. As anticipated, the mixed-anion concept has been proven to be of great help in facilitating methanol synthesis on the oxide surface.

Anion doping has also been important in the field of photocatalysis, known to be a useful means of activating metal oxides such as TiO$_2$ toward visible light responsiveness.[67−69] This is because doping metal oxides with anions that are less electronegative than oxygen provides a new energy state above the valence band formed by the 2p orbital of oxygen, narrowing the band gap.[22,70] N-doped TiO$_2$ with a visible light absorption band can reportedly be prepared with ease.[67] A discussion about the feasibility (e.g., thermodynamic and kinetic stability) of N-doped β-PtO$_2$ is presented in the Supporting Information. Based on it, we expect that N-doped β-PtO$_2$ can be synthesized.

Another difference to be noted in the energy diagram between Figures 4 and 8 is in the process of CH$_4$ adsorption. The adsorption of CH$_4$ onto the surface without doping is exothermic, while that onto the N-doped is endothermic. This implies that the doping of the surface with N makes the interaction between methane and the surface weaker. This is the Achilles heel of catalysts for methane: Nothing would start without methane adsorbed on the surface, but if the affinity of the surface for methane is too strong, CH$_3$ will just be strongly bound to the surface after the C−H bond cleavage, and no subsequent reaction is likely to occur. This is especially true for IrO$_2$, as discussed later. It would be very hard to satisfy both sides without being in a dilemma.

3.4. Comparison of the Structures with and without N Doping. Let us see how key intermediate structures vary depending on whether the surface is doped with N or not. In

Figure 9, we make a comparison of structures in the C−H bond dissociation process. When comparing **2** and **2′**, one can notice that the structural distortion of methane is larger in **2** than in **2′**; for example, the C−H bond to be dissociated is longer and the H−C−H angle directed toward the surface is wider. Since the deformation is a good measure of how much the methane is activated,[71,72] the nondoped β-PtO$_2$ surface can be regarded as more active for the C−H bond cleavage than the one doped with N. Indeed, the activation barrier for the C−H bond dissociation is larger on the N-doped than on the nondoped. Nevertheless, the activation barrier on the N-doped is about 4.5 kcal/mol at most, which is still deemed to be small when compared to that on the active catalyst of IrO$_2$.

When comparing **4** and **4′** in Figure 9, the C−Pt bond is longer on the N-doped than on the nondoped. This is indicative of the weakening of the bond as a result of the replacement of the axial O atom with a N atom, the result measuring up to our expectation.

Let us move on to a comparison of structures in the C−O bond formation (see Figure 10). At a first glance, the difference in geometry between the two looks very small. However, the difference in energetics is significant.

In the transition states (**7** and **7′**), the carbon atom has a trigonal planar geometry, which is specific to the methyl radical. If we assume that the instability of the system associated with methyl radical formation is comparable between the two, the difference in the activation energy can be attributed to the difference in the energy of the initial state.

It may also be important to note that the length of the Pt−N bond is shortened during the transition from state **6′** to state **7′**. In the nondoped system, there is also shrinkage of the corresponding Pt−O bond; however, the extent to which the bond is shortened is larger for the N-doped than for the nondoped. The destabilization associated with the cleavage of the Pt−C bond may be compensated somewhat by the
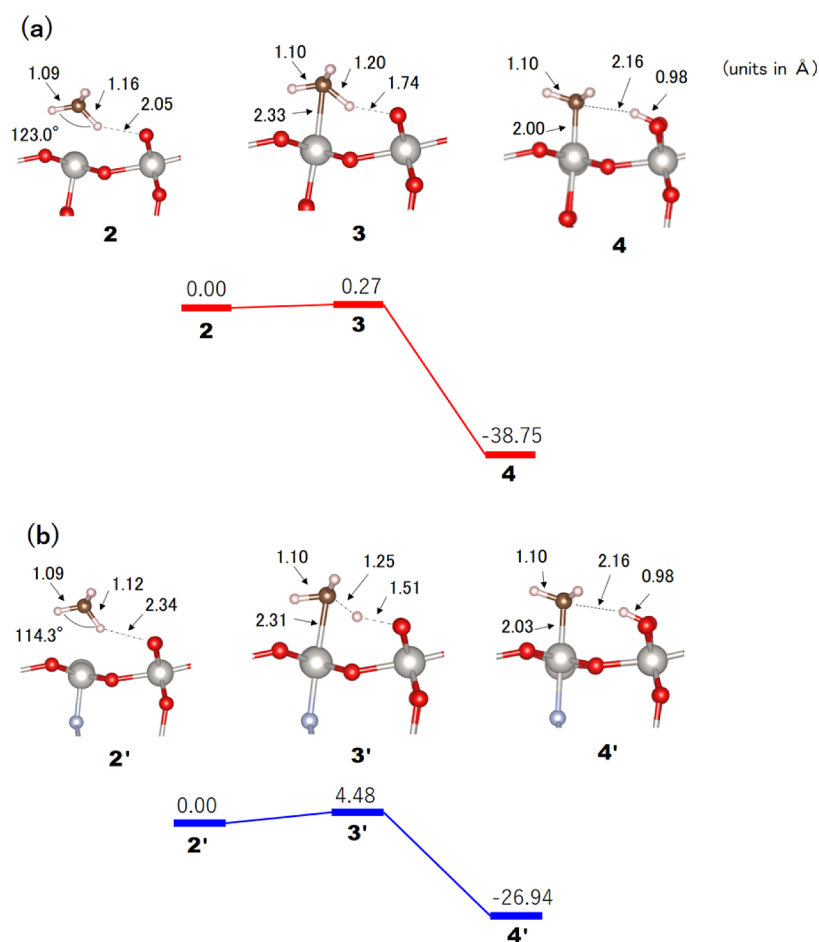
Figure 9. C−H bond dissociation reaction of methane on the (110) surface of β-PtO$_2$ (a) and that doped with N (b). The initial (**2** or **2′**), transition (**3** or **3′**), and final (**4** or **4′**) states are shown. These structures are numbered in accordance with those in Figures 4 and 8. Selected distances are shown in Å. The corresponding part of the potential energy diagram is shown below the structures, with the energy in the unit of kcal/mol referenced to that of the initial state (**2** or **2′**).

strengthening of the Pt−N bond. This also seems conducive to the lowering of the activation barrier in the N-doped.

3.5. Replenishment of the Oxygen Vacancy. Let us complete the catalytic cycle shown in Figure 1. Up to this point, we have simulated steps 1−4. Owing to the very high activation barrier of 47.9 kcal/mol for the C−O bond formation on the nondoped β-PtO$_2$ surface, methanol synthesis on the β-PtO$_2$ surface is unlikely to occur. However, when β-PtO$_2$ is doped with N, the activation barrier for the C−O bond formation is reduced to 27.7 kcal/mol, but the effects on the other activation barriers are less significant. Thus, methanol synthesis may occur on the doped surface, leaving an oxygen vacancy (V$_O$) behind.

The reduced V$_O$ site can be reoxidized by N$_2$O, resulting in gas-phase N$_2$ and restoring the lattice oxygen atom.[73] This process was simulated using the CI-NEB method for the N-doped surface, as shown in Figure 11. This figure indicates that the activation barrier associated with the regeneration of the catalyst is not high compared to that of the C−O bond formation. As such, the catalytic cycle can successfully be completed.

Although the activity of the Pt$_{cus}$ atom is crucial for the catalytic mechanism, the Pt$_{cus}$ atoms are not necessarily oxidized preferentially in the reoxidation of the catalyst. This is because the reduced V$_O$ site is more easily oxidized: the surface state where one Pt$_{cus}$ atom is oxidized with the V$_O$ site

left is higher in energy by about 2.5 eV than the one where the V$_O$ site is oxidized.

The first step of the catalysis, namely, the reduction of the catalytically active site, shown in Figure 8, is accompanied by an energy change of −6.93 kcal/mol. The second step, namely, the reoxidation of the catalyst, shown in Figure 11, is accompanied by an energy change of −25.8 kcal/mol. Thus, the overall energy change for the reaction of CH$_4$ + N$_2$O → CH$_3$OH + N$_2$ is −32.7 kcal/mol. Using the standard thermodynamic data,[74] one can obtain a change in the enthalpy of ca. −50.7 kcal/mol for this reaction. There seemingly is a discrepancy. However, one should note that the change in the total electronic energy calculated at 0 K with DFT cannot directly be compared with the enthalpy change observed in the experiment. This is because the zero-point energy coming from zero-point oscillations and the temperature-dependent vibrational energy are not taken into account.[75] Also, the density functional used may be critical for the results. A preceding PBE study for this reaction provided the overall energy change of about −38 kcal/mol,[76] which is consistent with our result. Could one use a hybrid functional, the energy difference would get closer to the experimental enthalpy difference, but there would still be a deviation of about 10 kcal/mol from the experimental value.[77]

3.6. Comparison with IrO$_2$. In our recent work on IrO$_2$,[24] we discussed a similar idea of controlling reactivity by anion
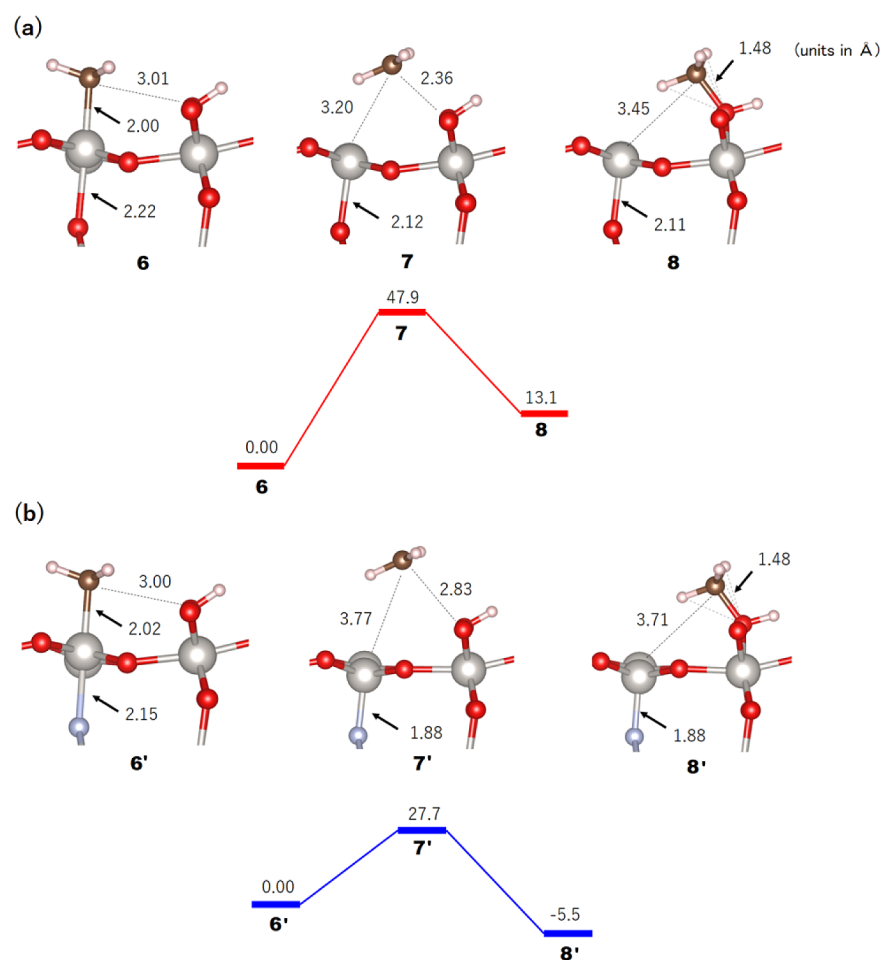
(a)

(b)

Figure 10. C−O bond formation reaction on the (110) surface of β-PtO$_2$ (a) and that doped with N (b). The initial (**6** or **6′**), transition (**7** or **7′**), and final (**8** or **8′**) states are shown. These structures are numbered in accordance with those in Figures 4 and 8. Selected distances are shown in Å. The corresponding part of the potential energy diagram is shown below the structures, with the energy in the unit of kcal/mol referenced to that of the initial state (**6** or **6′**).
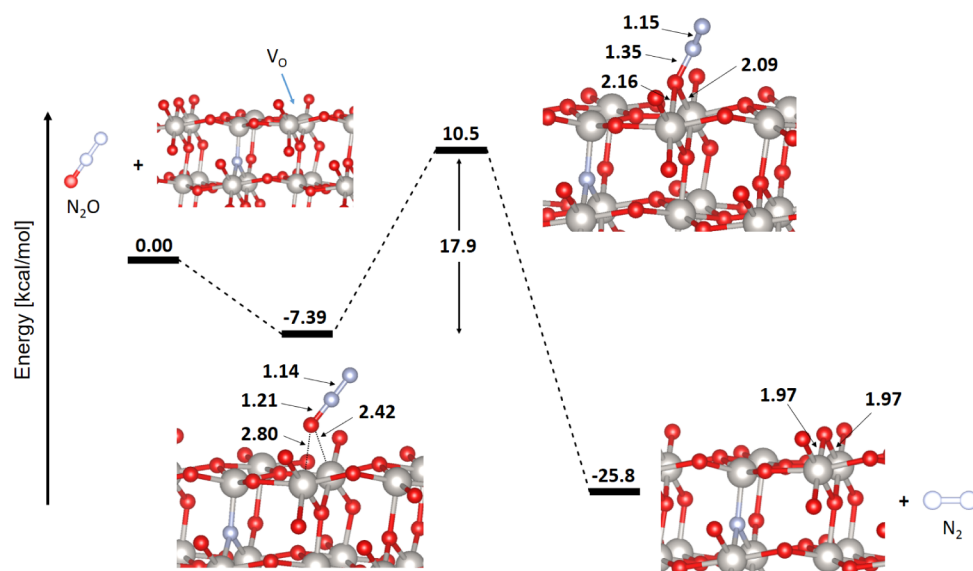

Figure 11. Calculated energy diagram for the reoxidation of the N-doped β-PtO$_2$ surface with an oxygen vacancy (V$_O$) by N$_2$O: first, the adsorption of N$_2$O occurs and then the N−O bond is dissociated with N$_2$ released. The numbers shown above the black bold horizontal lines representing intermediate states are their energies (in kcal/mol), which are calculated by taking the energy of the initial state as a reference. Selected distances are shown in Å.

doping, but the physical insights provided in this paper for β-PtO$_2$ cannot be drawn from the work on IrO$_2$. However, since the oxidation of methane on the surface of IrO$_2$ has been well studied experimentally,[8−11] IrO$_2$ may serve as a bridge to link our predictive theoretical study on β-PtO$_2$ with the experiment.

We calculated the activation energy of the C−O bond formation reaction on the (110) surface of IrO$_2$ using the same method as used for the calculations of the β-PtO$_2$ surface above. As shown in Figure 12, the activation energy of the C−
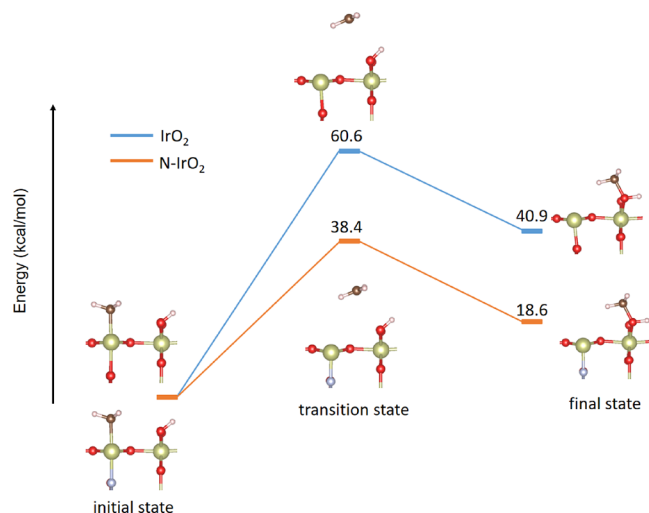

Figure 12. Calculated energy diagram for the C−O bond formation reaction on the (110) surfaces of IrO$_2$ (blue) and N-doped IrO$_2$ (orange). The numbers shown above the bold horizontal lines representing intermediate states are their energies (in kcal/mol), which are calculated by taking the energy of the initial state as a reference. Side views of the structures for the initial, transition, and final states are also shown.

O bond formation reaction on the IrO$_2$ surface is as high as 60.6 kcal/mol. This value is larger than that on the β-PtO$_2$ surface by about 13 kcal/mol. This is likely because of the fact that the Ir−C bond is stronger than the Pt−C bond.

To confirm the difference in the bond strength between Ir−C and Pt−C, we calculated the binding energy of CH$_3$ to the surface, defined as follows:

$$E_{bind} = (E_{surf} + E_{CH_3}) - E_{surf+CH_3} \qquad (1)$$

where $E_{surf+CH_3}$ denotes the energy of the whole system where CH$_3$ is adsorbed on the surface, like the initial structure in Figure 12. E_{surf} and E_{CH_3}, respectively, denote the energies of the surface slab and CH$_3$ calculated separately by maintaining the geometry as it was in the adsorbed state. The CH$_3$-binding energies on the IrO$_2$ and β-PtO$_2$ surfaces were calculated to be 3.2 and 2.4 eV, respectively. Indeed, the Ir−C bond was found to be stronger than the Pt−C bond.

By replacing the O atom in the axial position of the Ir atom with a N atom in the IrO$_2$ surface, the activation barrier is reduced by about 22 kcal/mol (see Figure 12). The amount of decrease in activation energy caused by N doping is almost the same as that on the β-PtO$_2$ surface. The original activation energy of the C−O bond formation reaction on the IrO$_2$ surface is so high that we have to conclude that the activation energy is indeed lowered by doping the surface with N but is still higher than that on the N-doped β-PtO$_2$ surface.

4. CONCLUSIONS

There is no report of methane being converted to methanol by the IrO$_2$ catalyst, but there is an experimental report that methane is converted to methanol by the IrO$_2$/CuO catalyst. The concept of the present study is to replace the roles of IrO$_2$ and CuO in the IrO$_2$/CuO catalyst by a single oxide. Based on the strength of the metal−oxygen bond in the oxide, we have proposed a catalyst of β-PtO$_2$. In our previous work regarding the C−H bond activation of methane on oxide surfaces, we actually made a theoretical prediction that β-PtO$_2$ would be more active than IrO$_2$. However, we did not predict anything about what occurs after the C−H bond is cleaved. In the present study, we have theoretically investigated whether a useful product of methane partial oxidation, i.e., methanol, can be formed on the surface of β-PtO$_2$ on the basis of the Mars−van Krevelen mechanism. Unfortunately, the activation barrier for the C−O bond formation process is so large, calculated to be 47.9 kcal/mol, that we have to conclude that this reaction is unlikely to occur. However, we never know when to give up, so we have made good use of techniques of orbital interaction analysis, such as COOP and FMO, to find out the origin of the very high activation energy. The strong Pt−C bond has been found to be the cause. The results of the orbital interaction analysis have suggested that the Pt−C bond can be destabilized by replacing the O atom in the axial position of the Pt atom with another element that has a lower electronegativity than O. To verify this, we have created a surface model in which the O atom is replaced with a N atom and calculated the energy profile of methanol synthesis. As a result, the activation energy of the rate-limiting step, the C−O bond formation process, has been greatly reduced to 27.7 kcal/mol. The magnitude of the activation barriers for the other stages of the reaction has hardly been affected, and it has been shown that the regeneration of the catalyst with N$_2$O can also occur with a relatively small activation energy.

■ ASSOCIATED CONTENT

Ⓢ Supporting Information

The Supporting Information is available free of charge at https://pubs.acs.org/doi/10.1021/acsomega.1c01476.

> Free-energy difference between α-PtO$_2$ and β-PtO$_2$, cell parameters of the optimized bulk structure of β-PtO$_2$, standard extended Hückel parameters used in this study, qualitative understanding of the molecular orbital spectrum for $[PtO_5]^{6-}$, feasibility of N-doped β-PtO$_2$, and atomic coordinates of optimized slab model structures (PDF)

■ AUTHOR INFORMATION

Corresponding Authors

Yuta Tsuji − *Institute for Materials Chemistry and Engineering and IRCCS, Kyushu University, Fukuoka 819-0395, Japan;* ⓞ orcid.org/0000-0003-4224-4532; Email: yuta@ms.ifoc.kyushu-u.ac.jp

Kazunari Yoshizawa − *Institute for Materials Chemistry and Engineering and IRCCS, Kyushu University, Fukuoka 819-0395, Japan;* ⓞ orcid.org/0000-0002-6279-9722; Email: kazunari@ms.ifoc.kyushu-u.ac.jp

Author

Keita Kurino − *Institute for Materials Chemistry and Engineering and IRCCS, Kyushu University, Fukuoka 819-0395, Japan*

Complete contact information is available at:
https://pubs.acs.org/10.1021/acsomega.1c01476

Notes

The authors declare no competing financial interest.

■ REFERENCES

(1) Liu, B. S.; Tian, L.; Li, L.; Au, C. T.; Cheung, A. S.-C. Performance of 3%Mo/ZSM-5 Catalyst in the Presence of Water during Methane Aromatization in Supersonic Jet Expansion. *AIChE J.* **2011**, *57*, 1852−1859.

(2) Yoshizawa, K. *Direct Hydroxylation of Methane*; Springer: Singapore, 2020.

(3) Tang, P.; Zhu, Q.; Wu, Z.; Ma, D. Methane Activation: The Past and Future. *Energy Environ. Sci.* **2014**, *7*, 2580−2591.

(4) Zakaria, Z.; Kamarudin, S. K. Direct Conversion Technologies of Methane to Methanol: An Overview. *Renewable Sustainable Energy Rev.* **2016**, *65*, 250−261.

(5) Luk, H. T.; Mondelli, C.; Ferré, D. C.; Stewart, J. A.; Pérez-Ramírez, J. Status and Prospects in Higher Alcohols Synthesis from Syngas. *Chem. Soc. Rev.* **2017**, *46*, 1358−1426.

(6) Busby, R. L. *Hydrogen and Fuel Cells*; Pennwell Corporation: Tulsa, 2005.

(7) Yang, L.; Ge, X. Chapter Three: Biogas and Syngas Upgrading. In *Advances in Bioenergy*; Li, Y., Ge, X., Eds.; Elsevier: New York, 2016; Vol. *1*, pp 125−188.

(8) Weaver, J. F. Surface Chemistry of Late Transition Metal Oxides. *Chem. Rev.* **2013**, *113*, 4164−4215.

(9) Weaver, J. F.; Hakanoglu, C.; Antony, A.; Asthagiri, A. Alkane Activation on Crystalline Metal Oxide Surfaces. *Chem. Soc. Rev.* **2014**, *43*, 7536−7547.

(10) Liang, Z.; Li, T.; Kim, M.; Asthagiri, A.; Weaver, J. F. Low-Temperature Activation of Methane on the IrO_2 (110). *Science* **2017**, *356*, 299−303.

(11) Kim, M.; Franklin, A.; Martin, R.; Feng, F.; Li, T.; Liang, Z.; Asthagiri, A.; Weaver, J. Adsorption and Oxidation of CH_4 on Oxygen-Rich IrO_2(110). *J. Phys. Chem. C* **2019**, *123*, 27603−27614.

(12) Yang, L.; Huang, J.; Ma, R.; You, R.; Zeng, H.; Rui, Z. Metal-Organic Framework-Derived IrO_2/CuO Catalyst for Selective Oxidation of Methane to Methanol. *ACS Energy Lett.* **2019**, *4*, 2945−2951.

(13) Cao, Y.; Saito, A.; Kobayashi, Y.; Ubukata, H.; Tang, Y.; Kageyama, H. Vanadium Hydride as an Ammonia Synthesis Catalyst. *ChemCatChem* **2021**, *13*, 191−195.

(14) Jain, A.; Ong, S. P.; Hautier, G.; Chen, W.; Richards, W. D.; Dacek, S.; Cholia, S.; Gunter, D.; Skinner, D.; Ceder, G.; Persson, K. A. Commentary: The Materials Project: A Materials Genome Approach to Accelerating Materials Innovation. *APL Mater.* **2013**, *1*, No. 011002.

(15) Tsuji, Y.; Yoshizawa, K. Adsorption and Activation of Methane on the (110) Surface of Rutile-Type Metal Dioxides. *J. Phys. Chem. C* **2018**, *122*, 15359−15381.

(16) Ciuparu, D.; Pfefferle, L. Contributions of Lattice Oxygen to the Overall Oxygen Balance during Methane Combustion over PdO-Based Catalysts. *Catal. Today* **2002**, *77*, 167−179.

(17) Stotz, H.; Maier, L.; Boubnov, A.; Gremminger, A. T.; Grunwaldt, J.-D.; Deutschmann, O. Surface Reaction Kinetics of Methane Oxidation over PdO. *J. Catal.* **2019**, *370*, 152−175.

(18) Mars, P.; Van Krevelen, D. W. Oxidations Carried Out by Means of Vanadium Oxide Catalysts. *Chem. Eng. Sci.* **1954**, *3*, 41−59.

(19) Kamer, P.; Vogt, D.; Thybaut, J. W. *Contemporary Catalysis: Science, Technology and Applications*; Royal Society of Chemistry: London, 2017.

(20) Burrington, J. D. *Industrial Catalysis: Chemistry and Mechanism*; Imperial College Press: London, 2016.

(21) Jupille, J.; Thornton, G. *Defects at Oxide Surfaces*; Springer: Heidelberg, 2015.

(22) Kageyama, H.; Hayashi, K.; Maeda, K.; Attfield, J. P.; Hiroi, Z.; Rondinelli, J. M.; Poeppelmeier, K. R. Expanding Frontiers in Materials Chemistry and Physics with Multiple Anions. *Nat. Commun.* **2018**, *9*, No. 772.

(23) Kageyama, H.; Yajima, T.; Tsujimoto, Y.; Yamamoto, T.; Tassel, C.; Kobayashi, Y. Exploring Structures and Properties through Anion Chemistry. *Bull. Chem. Soc. Jpn.* **2019**, *92*, 1349−1357.

(24) Tsuji, Y.; Yoshizawa, K. Mixed-Anion Control of C−H Bond Activation of Methane on the IrO_2 Surface. *J. Phys. Chem. C* **2020**, *124*, 17058−17072.

(25) Muller, O.; Roy, R. Formation and Stability of the Platinum and Rhodium Oxides at High Oxygen Pressures and the Structures of Pt_3O_4, $β$-PtO_2 and RhO_2. *J. Less-Common Met.* **1968**, *16*, 129−146.

(26) McBride, J. R.; Graham, G. W.; Peters, C. R.; Weber, W. H. Growth and Characterization of Reactively Sputtered Thin-Film Platinum Oxides. *J. Appl. Phys.* **1991**, *69*, 1596−1604.

(27) Shannon, R. D. Synthesis and Properties of Two New Members of the Rutile Family RhO_2 and PtO_2. *Solid State Commun.* **1968**, *6*, 139−143.

(28) Fernandez, M. P. H.; Chamberland, B. L. A New High Pressure Form of PtO_2. *J. Less-Common Met.* **1984**, *99*, 99−105.

(29) Zhuo, S.; Sohlberg, K. Platinum Dioxide Phases: Relative Thermodynamic Stability and Kinetics of Inter-Conversion from First-Principles. *Phys. B* **2006**, *381*, 12−19.

(30) Nomiyama, R. K.; Piotrowski, M. J.; Da Silva, J. L. F. Bulk Structures of PtO and PtO_2 from Density Functional Calculations. *Phys. Rev. B* **2011**, *84*, No. 100101.

(31) Chen, Q.; Yang, Y. Ab Initio Thermodynamics Studies on the Phase Stability of PtO_2 under Ambient and High-Pressure Conditions. *Comput. Mater. Sci.* **2020**, *180*, No. 109708.

(32) Seriani, N.; Jin, Z.; Pompe, W.; Ciacchi, L. C. Density Functional Theory Study of Platinum Oxides: From Infinite Crystals to Nanoscopic Particles. *Phys. Rev. B* **2007**, *76*, No. 155421.

(33) Kresse, G.; Hafner, J. Ab Initio Molecular Dynamics for Liquid Metals. *Phys. Rev. B: Condens. Matter Mater. Phys.* **1993**, *47*, 558−561.

(34) Kresse, G.; Hafner, J. Ab Initio Molecular-Dynamics Simulation of the Liquid-Metal-Amorphous-Semiconductor Transition in Germanium. *Phys. Rev. B: Condens. Matter Mater. Phys.* **1994**, *49*, 14251−14269.

(35) Kresse, G.; Furthmüller, J. Efficiency of Ab-Initio Total Energy Calculations for Metals and Semiconductors Using a Plane-Wave Basis Set. *Comput. Mater. Sci.* **1996**, *6*, 15−50.

(36) Kresse, G.; Furthmüller, J. Efficient Iterative Schemes for Ab Initio Total-Energy Calculations Using a Plane-Wave Basis Set. *Phys. Rev. B: Condens. Matter Mater. Phys.* **1996**, *54*, 11169−11186.

(37) Perdew, J. P.; Burke, K.; Ernzerhof, M. Generalized Gradient Approximation Made Simple. *Phys. Rev. Lett.* **1996**, *77*, 3865−3868.

(38) Blöchl, P. E. Projector Augmented-Wave Method. *Phys. Rev. B: Condens. Matter Mater. Phys.* **1994**, *50*, 17953−17979.

(39) Kresse, G.; Joubert, D. From Ultrasoft Pseudopotentials to the Projector Augmented-Wave Method. *Phys. Rev. B: Condens. Matter Mater. Phys.* **1999**, *59*, 1758−1775.

(40) Yang, Y.; Sugino, O.; Ohno, T. Band Gap of β-PtO$_2$ from First-Principles. *AIP Adv.* **2012**, *2*, No. 022172.

(41) Dudarev, S. L.; Botton, G. A.; Savrasov, S. Y.; Humphreys, C. J.; Sutton, A. P. Electron-Energy-Loss Spectra and the Structural Stability of Nickel Oxide: An LSDA+U Study. *Phys. Rev. B* **1998**, *57*, 1505−1509.

(42) Momma, K.; Izumi, F. VESTA 3 for Three-Dimensional Visualization of Crystal, Volumetric and Morphology Data. *J. Appl. Crystallogr.* **2011**, *44*, 1272−1276. VESTA is freely available https://jp-minerals.org/vesta/en/ (accessed 2021-5-12).

(43) Butcher, D. R.; Grass, M. E.; Zeng, Z.; Askoy, F.; Bluhm, H.; Li, W.-X.; Mun, B. S.; Somorjai, G. A.; Liu, Z. In Situ Oxidation Study of Pt (110) and Its Interaction with CO. *J. Am. Chem. Soc.* **2011**, *133*, 20319−20325.

(44) Li, D.; Matanovic, I.; Lee, A. S.; Park, E. J.; Fujimoto, C.; Chung, H. T.; Kim, Y. S. Phenyl Oxidation Impacts the Durability of Alkaline Membrane Water Electrolyzer. *ACS Appl. Mater. Interfaces* **2019**, *11*, 9696−9701.

(45) Yang, Y. Structural and Dynamical Properties of Water Adsorption on PtO$_2$(001). *RSC Adv.* **2018**, *8*, 15078−15086.

(46) Yang, Y.; Kawazoe, Y. Adsorption and Diffusion of H Atoms on β-PtO$_2$ Surface: The Role of Nuclear Quantum Effects. *J. Phys. Chem. C* **2019**, *123*, 13804−13811.

(47) Gong, X.-Q.; Raval, R.; Hu, P. General Insight into CO Oxidation: A Density Functional Theory Study of the Reaction Mechanism on Platinum Oxides. *Phys. Rev. Lett.* **2004**, *93*, No. 106104.

(48) Jacob, T. Theoretical Investigations on the Potential-Induced Formation of Pt-Oxide Surfaces. *J. Electroanal. Chem.* **2007**, *607*, 158−166.

(49) Diebold, U. The Surface Science of Titanium Dioxide. *Surf. Sci. Rep.* **2003**, *48*, 53−229.

(50) Henkelman, G.; Uberuaga, B. P.; Jónsson, H. A Climbing Image Nudged Elastic Band Method for Finding Saddle Points and Minimum Energy Paths. *J. Chem. Phys.* **2000**, *113*, 9901−9904.

(51) Jónsson, H.; Mills, G.; Jacobsen, K. W. Nudged Elastic Band Method for Finding Minimum Energy Paths of Transitions. In *Classical and Quantum Dynamics in Condensed Phase Simulations*; Berne, B. J., Ciccotti, G., Coker, D. F., Eds.; World Scientific: Singapore, 1998; pp 385−404.

(52) Henkelman, G.; Jónsson, H. Improved Tangent Estimate in the Nudged Elastic Band Method for Finding Minimum Energy Paths and Saddle Points. *J. Chem. Phys.* **2000**, *113*, 9978−9985.

(53) The transition state tools implementation for VASP is available at http://theory.cm.utexas.edu/vtsttools/ (accessed 2020-11-27).

(54) Pulay, P. Convergence Acceleration of Iterative Sequences. The Case of SCF Iteration. *Chem. Phys. Lett.* **1980**, *73*, 393−398.

(55) Hughbanks, T.; Hoffmann, R. Chains of Trans-Edge-Sharing Molybdenum Octahedra: Metal-Metal Bonding in Extended Systems. *J. Am. Chem. Soc.* **1983**, *105*, 3528−3537.

(56) Hoffmann, R. *Solids and Surfaces: A Chemist's View of Bonding in Extended Structures*; Wiley-VCH: Weinheim, 1988.

(57) Mulliken, R. S. Electronic Population Analysis on LCAO-MO Molecular Wave Functions. I. *J. Chem. Phys.* **1955**, *23*, 1833−1840.

(58) Song, W. X.; Zhao, S. J. Spin Polarization Gives Rise to Cu Precipitation in Fe-Matrix. *Phys. Chem. Chem. Phys.* **2014**, *16*, 7222−7230.

(59) Landrum, G. A.; Glassey, W. V. *YAeHMOP: Yet Another extended Huckel Molecular Orbital Package*, version 3.0, 2018. http://yaehmop.sourceforge.net/ (accessed 2020-11-27).

(60) Avery, P.; Ludowieg, H.; Autschbach, J.; Zurek, E. Extended Hückel Calculations on Solids Using the Avogadro Molecular Editor and Visualizer. *J. Chem. Educ.* **2018**, *95*, 331−337.

(61) Alvarez, S. *Table of Parameters for Extended Hückel Calculations*; Universitat de Barcelona: Barcelona, 1993.

(62) Tsuji, Y.; Saito, M.; Yoshizawa, K. Dynamics and Energetics of Methane on the Surfaces of Transition Metal Oxides. In *Direct Hydroxylation of Methane*; Yoshizawa, K., Ed.; Springer: Singapore, 2020; pp 101−133.

(63) Viewkel is part of the YAeHMOP suite of programs. Landrum, G. A. *YAeHMOP: Yet Another Extended Huckel Molecular Orbital Package*, 2018. YAeHMOP is freely available http://yaehmop.sourceforge.net/ (accessed 2020-11-27).

(64) *Atomistix ToolKit*, version 2019; QuantumWise A/S, 2019.

(65) Weaver, J. F.; Carlsson, A. F.; Madix, R. J. The Adsorption and Reaction of Low Molecular Weight Alkanes on Metallic Single Crystal Surfaces. *Surf. Sci. Rep.* **2003**, *50*, 107−199.

(66) Mahyuddin, M. H.; Shiota, Y.; Yoshizawa, K. Methane Selective Oxidation to Methanol by Metal-Exchanged Zeolites: A Review of Active Sites and Their Reactivity. *Catal. Sci. Technol.* **2019**, *9*, 1744−1768.

(67) Miyoshi, A.; Nishioka, S.; Maeda, K. Water Splitting on Rutile TiO$_2$-Based Photocatalysts. *Chem. − Eur. J.* **2018**, *24*, 18204−18219.

(68) Sato, S. Photocatalytic Activity of NO$_x$-Doped TiO$_2$ in the Visible Light Region. *Chem. Phys. Lett.* **1986**, *123*, 126−128.

(69) Asahi, R.; Morikawa, T.; Ohwaki, T.; Aoki, K.; Taga, Y. Visible-Light Photocatalysis in Nitrogen-Doped Titanium Oxides. *Science* **2001**, *293*, 269−271.

(70) Ansari, S. A.; Khan, M. M.; Ansari, M. O.; Cho, M. H. Nitrogen-Doped Titanium Dioxide (N-Doped TiO$_2$) for Visible Light Photocatalysis. *New J. Chem.* **2016**, *40*, 3000−3009.

(71) Shestakov, A. F.; Shilov, A. E. Five-Coordinate Carbon Hydroxylation Mechanism. *J. Mol. Catal. A: Chem.* **1996**, *105*, 1−7.

(72) Yoshizawa, K.; Ohta, T.; Yamabe, T.; Hoffmann, R. Dioxygen Cleavage and Methane Activation on Diiron Enzyme Models: A Theoretical Study. *J. Am. Chem. Soc.* **1997**, *119*, 12311−12321.

(73) *Handbook of Advanced Methods and Processes in Oxidation Catalysis*; Duprez, D., Cavani, F., Eds.; Imperial College Press: London, 2014.

(74) Heats of formation of CH$_4$, N$_2$O, and CH$_3$OH were taken from the NIST Chemistry WebBook. https://webbook.nist.gov/chemistry/ (accessed 2021-4-14).

(75) Velikokhatnyi, O. I.; Kumta, P. N. Energetics of the Lithium-Magnesium Imide-Magnesium Amide and Lithium Hydride Reaction for Hydrogen Storage: An Ab Initio Study. *Mater. Sci. Eng., B* **2007**, *140*, 114−122.

(76) Mahyuddin, M. H.; Shiota, Y.; Staykov, A.; Yoshizawa, K. Theoretical Investigation of Methane Hydroxylation over Isoelectronic [FeO]$^{2+}$- and [MnO]$^+$-Exchanged Zeolites Activated by N$_2$O. *Inorg. Chem.* **2017**, *56*, 10370−10380.

(77) Abe, T.; Kametani, Y.; Yoshizawa, K.; Shiota, Y. Mechanistic Insights into the Dicopper-Complex-Catalyzed Hydroxylation of Methane and Benzene Using Nitric Oxide: A DFT Study. *Inorg. Chem.* **2021**, *60*, 4599−4609.